Three-Dimensional Transient Flow of Spin-Up in a Filled Cylinder with Oblique Gravity Force

By

R. J. HUNG and H. L. PAN

Reprinted from

TRANSACTIONS OF THE JAPAN SOCIETY FOR
AERONAUTICAL AND SPACE SCIENCES

VOL. 38, NO. 120, 1995

Three-Dimensional Transient Flow of Spin-Up in a Filled Cylinder with Oblique Gravity Force*

By R. J. HUNG** and H. L. PAN**

Key Words: Three-Dimensional Transient Flow, Cylinder, Gravity Force

Abstract

Three-dimensional transient flow profiles of spin-up in a fully liquid filled cylinder from rest with gravity acceleration at various directions are numerically simulated and studied. Particular interests are concentrated on the development of temporary reverse flow zones and Ekman layer right after the impulsive start of spin-up from rest, and decay before the flow reaching to the solid rotation. Relationship of these flow developments and differences in the Reynolds numbers of the flow and its size selection of grid points concerning the numerical instabilities of flow computations are also discussed. In addition to the gravitational acceleration along the axial direction of cylindrical container, a series of complicated flow profiles accompanied by three-dimensional transient flows with oblique gravitational acceleration has been studied.

1. Introduction

Time-dependent, three-dimensional numerical procedures for solving Navier-Stokes equations with moving boundaries which are capable to study sloshing dynamics dominated by capillary effect have been developed.[1-10] One of the objectives of this work is to test the applicability of these numerical codes for the case of transient spin-up flow occurring in a cylindrical container when it is suddenly rotated about its longitudinal axis. Knowledge of this internal flow is needed to design spacecraft dewar containers which carry cryogenic propellant and are required to spin-up to certain speeds for instrument calibration when the spacecrafts are placed to the orbit, and then spin-down to another speed for the spacecraft normal operation.[11] It is also required by other flying objects such as gun-launched projectiles which carry smoke/incendiary agents or chemical payloads. Liquid payloads enhance spin decay of projectiles,[12,13] and their presence can produce flight dynamic instabilities as a result of reasonance between the projectiles mutational motion and inertial oscillations in the rotating liquid.[14-18] From a computational view point, this problem is instructive because it is an example of a class of internal flow problems for which computational experiments can uncover details of the flow that can not be easily visualized or measured experimentally.

In this study, we are particularly interested in the study of dynamical flow zone

* Received August 26th, 1994.

** Department of Mechanical and Aerospace Engineering, College of Engineering, The University of Alabama in Huntsville, Huntsville, Alabama 35899, U.S.A.

7) Shoji, T. and Kimura, I.: Thermal and Ionization Nonequilibrium in Magnetoplasmadynamic Flows, *Trans. Japan Soc. Aero. Space Sci.*, **35**, 109 (1992), pp. 107–118.
8) Sheppard, E. and Martinez-Sanchez, M.: Ionization Rate Models and Inlet Ignition in Self-Field MPD Thrusters, 23rd International Electric Propulsion Conference, Seattle, Washington, 1993, IEPC-93-071.
9) Burton, R. L. and Tiliakos, N.: Injected Propellant Ionization in MPD Thrusters, *J. Propul. Power*, **9**, 5 (1993), pp. 764–770.
10) Choueiri, E. Y. and Okuda, H.: Anomalous Ionization in the MPD Thruster, 23rd International Electric Propulsion Conference, Seattle, Washington, 1993, IEPC-93-067.
11) Spitzer, L., Jr.: *Physics of Fully Ionized Gases*, 2nd ed., Interscience Publishers, New York, 1962.

development right after the impulsive start of container spin-up from rest. In otherwords, the development and decay of temporary reverse flow regions and Ekman layer at the beginning of container spin-up before the flow reaching to the solid flow conditions will be studied. It is also interesting to investigate (a) the relationship between these flow zone (including reverse flow and Ekman layer) developments and the Reynolds number of flow profiles, and also (b) the relationship between the size selection of grid points with respect to the Reynolds number and the development of numerical instabilities in computing flow fields.

2. Governing Equations and Boundary Conditions

Consider a closed circular cylindrical container of radius R, with height, H, which is fully filled with liquid water of constant density ρ and viscosity μ. Let us use cylindrical coordinates (r, θ, z), with corresponding velocity components (u, v, w), and corresponding gravitational acceleration components (g_r, g_θ, g_z). The time-dependent and three dimensional mathematical formulation is adopted. The governing equations are shown as follows:

(A) Continuity Equation

$$\frac{1}{r}\frac{\partial}{\partial r}(ru)+\frac{1}{r}\frac{\partial v}{\partial \theta}+\frac{\partial w}{\partial z}=0 \qquad \ldots.(1)$$

(B) Momentum Equations

$$\rho\left(\frac{\partial u}{\partial t}+u\frac{\partial u}{\partial r}+\frac{v}{r}\frac{\partial u}{\partial \theta}-\frac{v^2}{r}+w\frac{\partial u}{\partial z}\right)=-\frac{\partial p}{\partial r}+\rho g_r+\mu\left(\nabla^2 u-\frac{u}{r^2}-\frac{2}{r^2}\frac{\partial v}{\partial \theta}\right) \qquad \ldots.(2)$$

$$\rho\left(\frac{\partial v}{\partial t}+u\frac{\partial v}{\partial r}+\frac{v}{r}\frac{\partial v}{\partial \theta}+\frac{uv}{r}+w\frac{\partial v}{\partial z}\right)=-\frac{1}{r}\frac{\partial p}{\partial \theta}+\rho g_\theta+\mu\left(\nabla^2 v-\frac{v}{r^2}+\frac{2}{r^2}\frac{\partial u}{\partial \theta}\right) \qquad \ldots.(3)$$

$$\rho\left(\frac{\partial w}{\partial t}+u\frac{\partial w}{\partial r}+\frac{v}{r}\frac{\partial w}{\partial \theta}+w\frac{\partial w}{\partial z}\right)=-\frac{\partial p}{\partial z}+\rho g_z+\mu\nabla^2 w \qquad \ldots.(4)$$

where

$$\nabla^2=\frac{1}{r}\frac{\partial}{\partial r}\left(r\frac{\partial}{\partial r}\right)+\frac{1}{r^2}\frac{\partial^2}{\partial \theta^2}+\frac{\partial^2}{\partial z^2} \qquad \ldots.(5)$$

The initial conditions for the flow parameters before rotation are

$$u=v=w=0 \quad \text{at} \quad t<0 \qquad \ldots.(6)$$

At time $t=0$, cylindrical container is suddenly rotated about its longitudinal axis to rotation speed ω. The boundary conditions become

$$\left.\begin{aligned} u=w=0 \\ v=R\omega \end{aligned}\right\} \quad \text{at} \quad r=R \quad \text{and} \quad t\geq 0 \qquad \ldots.(7)$$

$$\left.\begin{aligned} u=w=0 \\ v=r\omega \end{aligned}\right\} \quad \text{at} \quad z=0 \quad \text{and} \quad t\geq 0 \qquad \ldots.(8)$$

$$\left.\begin{aligned} u=w=0 \\ v=r\omega \end{aligned}\right\} \quad \text{at} \quad z=H \quad \text{and} \quad t\geq 0 \qquad \ldots\ldots(9)$$

In this study, a cylindrical container with a radius of 3 cm and a height of 2 cm has been used in the numerical simulation. Following data was used at temperature of 20°C: liquid water density = 997.3 kg/m^3, fluid pressure = 1.013×10^5 N/m^2, liquid water viscosity coefficient = 1.006×10^{-6} m^2/s, and under $1g_0$ ($=9.81$ m/s^2) gravitational acceleration.

The computer algorithms employed in this study have been developed and illustrated in our earlier studies,[19-21] and will not be repeated in this paper. The time step is determined automatically based on the size of grid points and the velocity of flow fields. As the thickness of boundary layer is inversely proportional to the square root of Reynolds number, size of grid points shall be adjusted according to the flow fields of Reynolds number. In other words, the size of grid points shall be smaller as the flow fields of Reynolds number becomes greater. Fail of adjusting the size of grid points based on the increasing of Reynolds number will result in the numerical instability to the extreme severity of the local oscillations.[13] Special care shall be attempted to eliminate these numerical instabilities by properly adjusting the size of grid points which eventually contribute to the adjustment of time steps. It is needless to say that the development of a real physical instability will certainly occur at the higher Reynolds number because of less viscosity effect contributing to the damping of flow disturbances. It is utterly important for us to distinguish the differences between numerical and real physical instabilities, particularly for the flows with high Reynolds number.

In this study, two rotating speeds with $\omega=102$ and 10.2 rpm are chosen. Reynolds numbers for $\omega=102$ and 10.2 rpm are 9.7×10^3 and 9.7×10^2, respectively. For the case of higher and lower Reynolds numbers, grids of $21\times34\times28$ and $16\times34\times14$, respectively, along (r, θ, z) coordinates were used. By using grids of $16\times34\times14$ in the computation of flows with higher Reynolds number, an extremely severe numerical instabilities of flow fields is resulted.

Components of background gravity shall be given by

$$g_i=(g_r, g_\theta, g_z)=g(\sin\psi\cos\theta, -\sin\psi\sin\theta, -\cos\psi) \qquad \ldots\ldots(10)$$

where g is the magnitude of background gravity, and ψ is the angle of background gravity between the direction of the container rotating axis and the direction of background gravity. In this study $\psi=0°$ and 60° along the r–z plane with $\theta=0°$ are chosen.

The average time step determined from the size of the grid points and velocity of flow fields for 102 and 10.2 rpm container rotating speed are 0.00108 and 0.01369 s, respectively, while the CPU time required by the supercomputer CRAY II to execute one time step is 1.32 and 0.392 s, respectively.

3. Transient Phenomena During Spin-Up from Rest

A series of numerical simulations of transient flow phenomena during container spin-up from rest with rotating speeds of 102 and 10.2 rpm is carried out.

(A) Spin-up With Normal Direction Gravitational Acceleration

In this case, a finer grids is chosen to avoid numerical instabilities because of higher Reynolds number flow fields with thinner boundary layer thickness. With gravity field along the rotating axis of container, all the flow fields are axis symmetric. Figure 1 (A) shows the transient velocity vectors along the circumferential direction in r–θ plane at height $z=1$ cm and ending with the status of solid rotation. Length of arrow illustrates the magnitude of circumferential velocity of fluid particles at the corresponding locations. With center of rotating axis as an origin, horizontal axes toward right hand and left hand sides are $\theta=0°$ and 180°, respectively, whereas vertical axes toward uphand and downhand are $\theta=90°$ and 270°, respectively. Notation of these illustrations cover throughout this paper. It shows an animation of a picking up of circumferential velocity profiles which propagate from the container wall during a sudden rotation from rest, gradually transmit the momentum inward and toward the center of the rotating axis through the viscosity effect. Finally, a near solid rotation is accomplished at the end of the time at $t=12.0$ s. Figure 1 (B) shows the similar animation of the circumferential velocity profiles with respect to time and the values along radial coordinate (in term of u/V where $V=R\omega$) at height $z=1$ cm and ending with solid rotation status. It shows clearly how flow momentum transmits from the side wall during sudden spin-up of container from rest, and gradually propagates the flow momentum inward and toward the container rotating axis. Finally, it reaches a near solid rotation at the end of $t=12.0$ s. The velocity profile becomes a straight line and it can be represented by the equation $v=\omega r$ as that shown at the end of simulation in Fig. 1 (B).

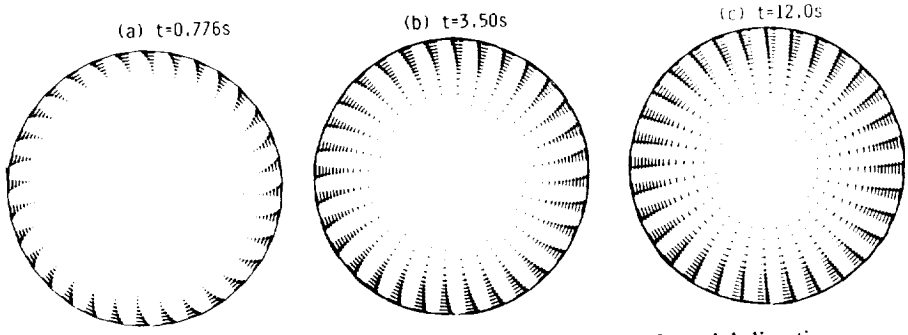

Fig. 1 (A). Transient velocity vectors along the circumferential direction in r–θ plane at height $z=1$ cm, $\omega=102$ rpm, and $\psi=0°$.

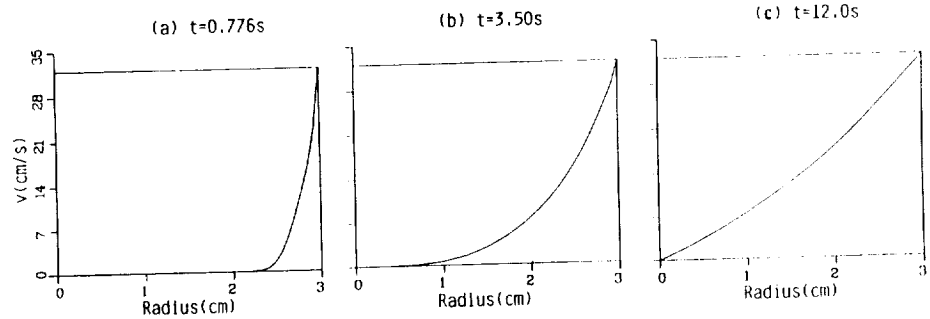

Fig. 1 (B). Transient circumferential velocity profiles with respect to time and radial coordinate at height $z=1$ cm, $\omega=102$ rpm and $\psi=0°$.

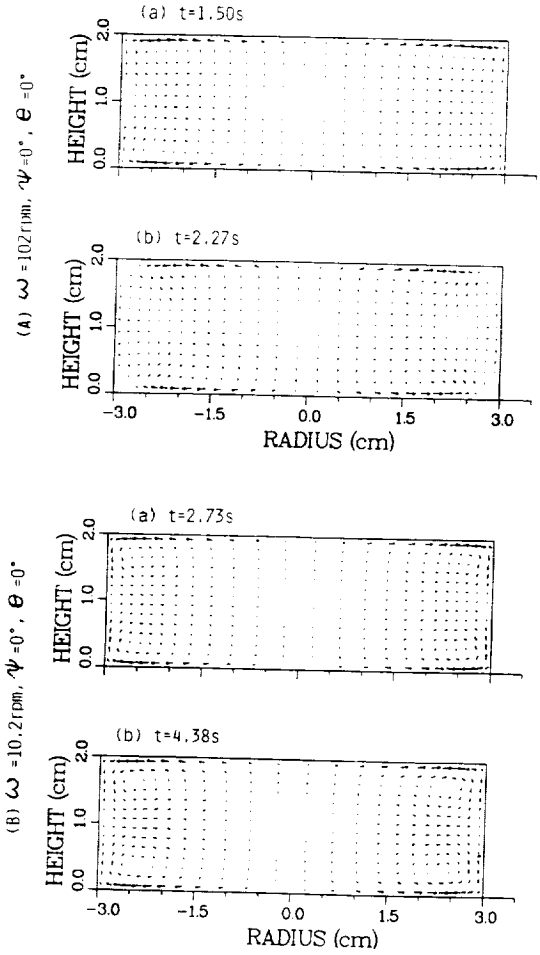

Fig. 2. (A) Animation of the formation of four temporary reverse flow zones at upper left, upper right, lower left, and lower right near the side walls with vectors of flow velocities in r–z plane at $r=2.40$ cm, $\omega=102$ rpm and $\psi=0°$. (B) Animation of the formation of four temporary reverse flow zones at upper left, upper right, lower left and lower right near the side walls with vector of flow velocities in r–z plane at the beginning of container spin-up from rest, $\omega=10.2$ rpm, and $\psi=0°$.

It is interesting to note the existence of temporary reverse flow regions near the sidewalls at the beginning of container spin-up from rest. Figure 2 (A) shows the animation of the formation of four temporary reverse flow zones at upper left, upper right, lower left, and lower right near the sidewalls of cylindrical container with vectors of flow velocities shown in r–z plane at the beginning of spin-up from rest. These reverse flow zones were initiated and developed after the impulsive start and became a full reverse flow at the beginning of spin-up and disappear quickly before the flow reaching to the status of solid rotation.

The reverse flow zones do not develop in the calculations for flow fields with low Reynolds number.[12] This is due to the facts of the flows with low Reynolds number characterized by a thicker boundary layer and a greater amount of viscous dissipation. For the flows with high Reynolds number, there are thinner boundary layer and less viscous dissipation present and initial effects become more pronounced. Fluid particles near the endwalls are accelerated radially outward in a spiral motion as the Ekman layer and boundary layer develop. These particles overshoot their "equilibrium radial position" before they turn upward (downward) from the edge of lower (upper) Ekman layer in r–z plane, or outside the boundary layer near the corner. The reverse flow zones, that develop along the sidewall, are apparently linked to the inertial oscillations developed as swirling fluid particles travel upward (downward) outside the boundary layer along the lower (upper) sidewall and begin to migrate radially inward [see Fig. 2 (A) for detail].

Development and decay of Ekman layer have been studied. Ekman layer is a layer in which there is a three-way balance between the Coriolis force, the pressure gradient force, and the viscous stress.[22] It is known that the Ekman layer solution is the fact that the flow velocity in the boundary layer has a component directed toward lower pressure. A sharp pressure gradient $\partial p/\partial r$ is developed right after the impulsive start of container spin-up from rest. This pressure gradient immediately induced a component

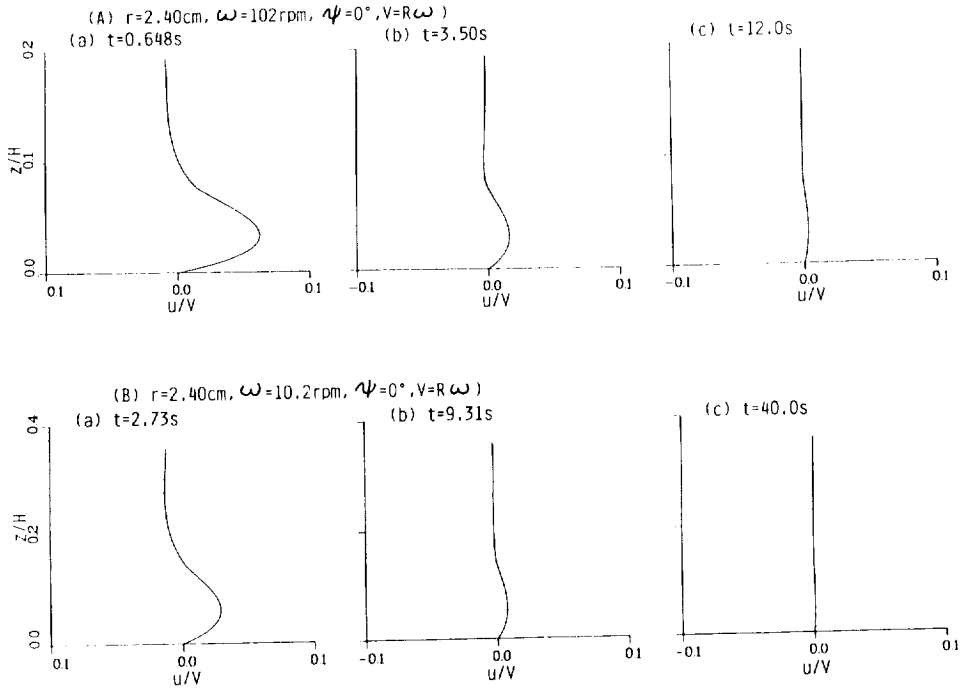

Fig. 3. (A) Animation of the development and decay of Ekman layer at lower right near the end wall of container in r–z plane at $r=2.40$ cm, $\omega=102$ rpm and $\psi=0°$. (B) Animation of the development and decay of Ekman layer at lower right near the side wall of container in r–z plane at $r=2.40$ cm, $\omega=10.2$ rpm, and $\psi=0°$.

of flow velocity along radial direction toward lower pressure side. Similar to four reverse flow zones shown in Fig. 2 (A), four flow zones of Ekman layers in r–z plane are also developed. Figure 3 (A) shows the animation of the development and decay of Ekman layer at lower right near the sidewall of container in r–z plane at $r=2.40$ cm and $\omega=102$ rpm. It shows that a pronounced Ekman layer is developed during the time period of 0.25 to 3.50 s with maximum peaks located at $z/H=0.03$ near the lower wall and at $z/H=0.97$ near the upperwall, and decays rapidly afterwards.

As indicate earlier, size of grid points shall be adjusted properly when Reynolds number of flow fields changes. In otherwords, grids of $16\times34\times14$, which are less finer than the previous case because of lower Reynolds number with thicker boundary layer thickness of flow profiles, are adopted. Figure 4 (A) shows the transient velocity vectors along the circumferential direction in r–θ plane at height $z=1$ cm for $\omega=10.2$ rpm, and ending with solid rotation status. Figure 4 (B) shows the similar animation of the circumferential velocity profiles with respect to time and the magnitude along radial coordinate (in term of u/V where $V=R\omega$) at height $z=1$ cm for $\omega=10.2$ rpm and ending with solid rotation status. Comparison of Figs. 1, and 2 for flows with spin-up speeds of 102 and 10.2 rpm, respectively, show that it takes longer time for lower spin-up speeds to reach a solid rotation status.

Existence of temporary reverse flow zones near the sidewalls at the beginning of container spin-up from rest for $\omega=10.2$ rpm is also examined. Figure 2 (B) shows the animation of four reverse flow zones from the initiation and the development after the

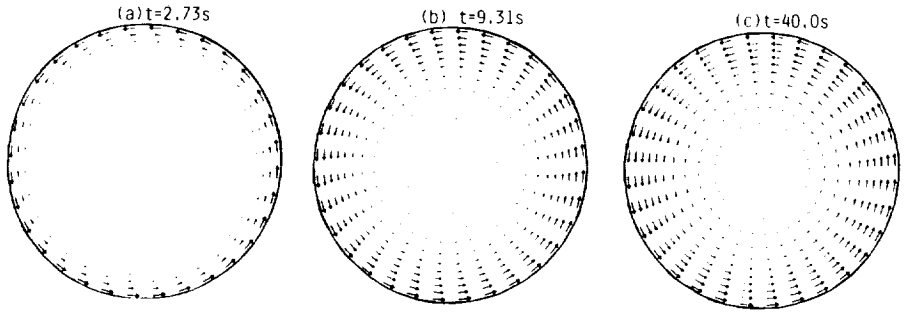

Fig. 4(A). Transient velocity vectors along the circumferential direction in r–θ plane at height $z=1$ cm, $\omega=10.2$ rpm and $\psi=0°$C.

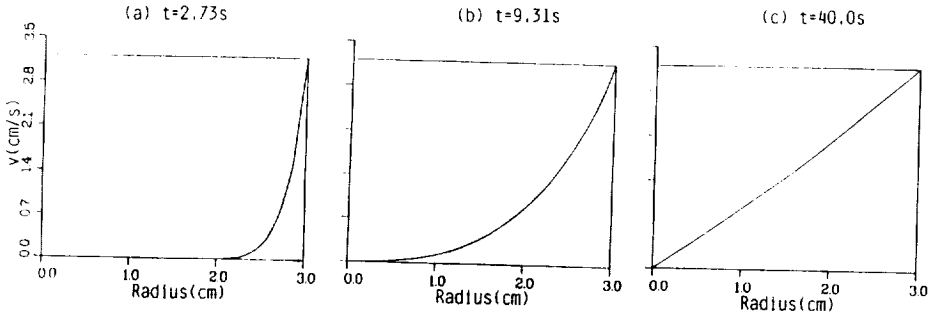

Fig. 4(B). Transient circumferential velocity profiles with respect to time and radial coordinates at height $z=1$ cm, $\omega=10.2$ rpm and $\psi=0°$.

impulsive start to a full reverse flow at the beginning of impulsive spin-up from rest. Again, these reverse flows disappear quickly before the flow reaching to the status of solid rotation. Comparison of Figs. 2 (A) and (B) between flows with spin-up speeds of 102 and 10.2 rpm, respectively, show that it takes a longer time of initiation, development and decay of reverse flow zones for lower spin-up speed than that of the higher spin-up speed. Computer experiments of several flow profiles with lower spin-up speeds than the case presented in this study indicate that there is no appearance of reverse flow zone during the flow spin-up motion with lower Reynolds number flows because of thicker boundary layer and a greater amount of viscous dissipation.

Development and decay of Ekman layer for spin-up speed with 10.2 rpm are examined. Figure 3 (B) shows the animation of Ekman layer at lower right near the sidewall of container at $r=2.40$ cm and $\omega=10.2$ rpm. It shows that a pronounced Ekman layer is developed during the time period of 0.65 to 11.2 s with maximum peak values of radial velocity located at $z/H=0.05$ near the lower wall and at $z/H=0.95$ near the upper wall, and decay rapidly afterwards. Comparison of Figs. 3 (A) and (B) between flows with spin-up speeds of 102 and 10.2 rpm, respectively, show that it takes a longer time for initiation and development of Ekman layer for lower spin-up speed than that of the higher spin-up speed. Locations of the maximum values of radial velocity for lower spin-up speed is with a distance further away from the side wall than that of the higher spin-up speed because boundary layer thickness of lower spin-up speed is thicker than that of the higher spin-up speed.

(B) Spin-up with Oblique Direction Gravitational Acceleration

Previous section describes the spin-up flow fields with gravitational acceleration pointing along the axial direction of rotating cylinder. In this section, gravitational acceleration acting on the spin-up cylinder with a direction $\psi=60^\circ$ measured counterclockwise from the rotating axis in r–z plane with $\theta=0^\circ$ have been studied. Order of magnitude comparison between centrifugal and gravitational accelerations show that the centrifugal accelerations for $\omega=102$ and 10.2 rpm are 342 and 34.2 cm/s^2, respectively, with 3 cm radius of cylinder against 981 cm/s^2 for gravitational acceleration. Obviously, it can be anticipated that the flow profiles will be greatly modified by the oblique direction of gravitational acceleration in comparison with normal direction for the case of 10.2 rpm spin-up rotation speed. In this study, computational results of 10.2 rpm sudden spin-up rotation speed from rest with 60° oblique direction of gravitational acceleration is presented and discussed.

Figure 5 shows the transient velocity vectors along the circumferential direction in r–θ plane at height $z=1$ cm for 60° oblique direction gravitational acceleration acting on the 10.2 rpm sudden spin-up filled cylinder from rest. Oblique direction gravitational acceleration drives the rotation flow in two sections: one with acceleration (flow direction coinsides with that of gravitational acceleration) from $\theta=180^\circ$ to 360°; and other with deacceleration (flow direction reverse to that of gravitational acceleration) from $\theta=0^\circ$ to 180°, both of the rotating flow in counter clockwise directions. It shows how the momentum transmits inward from the solid wall to the fluid propagating toward the center of rotating axis. Clearly, an asymmetric flow zone with uneven velocity distribution are created based on the driving forces of acceleration and deceleration activated by the oblique direction gravitational accelerations. At the end of simulation, it shows a steady state flow profile with normal direction gravitational acceleration, and there is

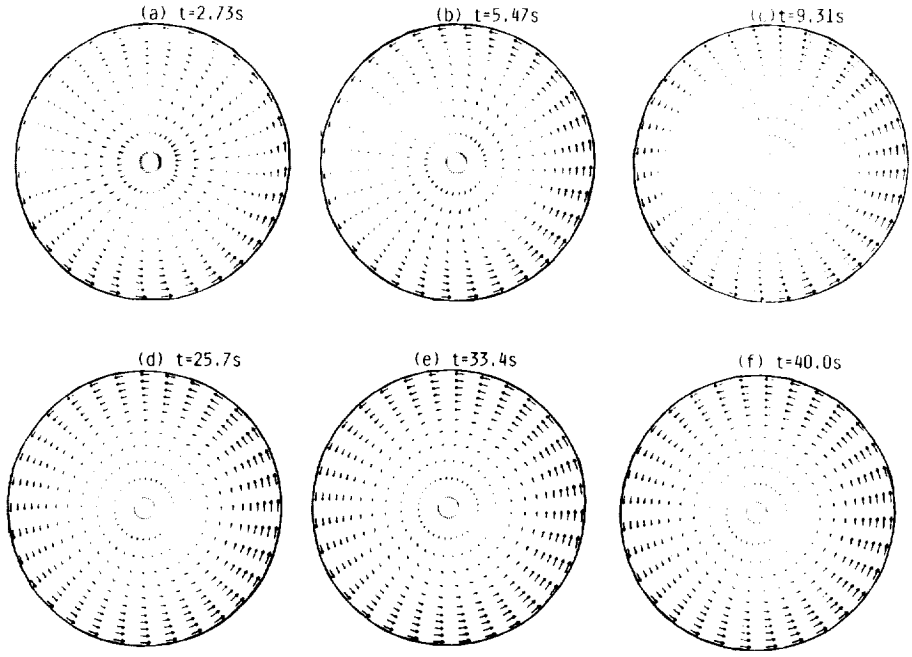

Fig. 5. Transient velocity vectors along the circumferential direction in r–θ plane at height $z=1$ cm and $\omega=10.2$ rpm for oblique gravitational acceleration ($\psi=60°$C).

a steady-state, but not solid-rotation flow pattern with oblique direction gravitational acceleration.

In order to show the differences in the animation of the circumferential velocity profiles (in term of u/V where $V=R\omega$) with respect to time and the magnitudes along radial coordinates at height $z=1$ cm for these separate flow zones, Figs. 6 and 7 show these flow profiles along $\theta=0°$ (acceleration zone), and $\theta=180°$ (deceleration zone), respectively. Comparison of Figs. 4 and 5–7 for spin-up flow profiles in circumferential component with gravitational acceleration along normal and oblique directions can draw the following conclusions: (a) solid-rotation flow profiles can be reached for spin-up flow with normal gravitational acceleration, whereas there is steady-state but not solid-rotation flow for that with oblique gravitational acceleration. (b) In the deceleration zone of spin-up from rest with oblique gravitational acceleration during the status of steady-state flow, there is a velocity hill (0.5 cm/s above solid rotation speed) near the center of rotating axis at $r=0.6$ cm, and velocity ditch (0.8 cm/s below solid rotation speed) near the end wall of cylinder at $r=2.9$ cm over which the flow velocity in circumferential component sharply increase to the magnitude of cylindrical wall velocity near the end walls. (c) In the acceleration zone of spin-up from rest with oblique gravitational acceleration during the status of steady-state flow, there is a velocity ditch (0.8 cm/s below solid rotation speed) near the center of rotating axis at $r=0.4$ cm, and velocity hill (0.5 cm/s above solid rotation speed, and also 0.3 cm/s above the magnitude of cylindrical end wall velocity of rotation) near the end wall of cylinder at $r=2.9$ cm over which the flow velocity in circumferential component decrease to the

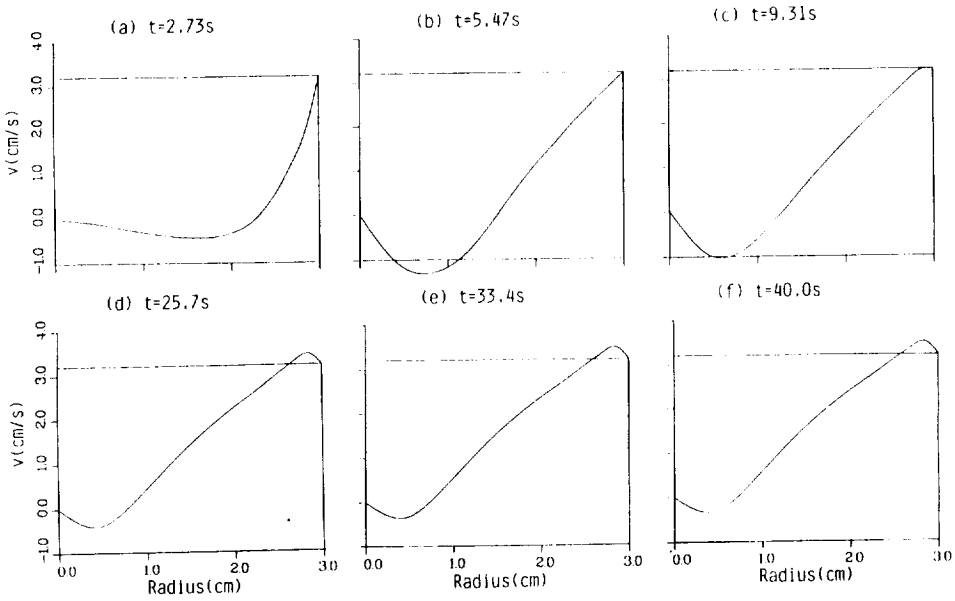

Fig. 6. Transient circumferential velocity profiles with respect to time and radial coordinate along $\theta = 0°$ (acceleration zone) at height $z = 1$ cm and $\omega = 10.2$ rpm, for oblique gravitational acceleration ($\psi = 60°$).

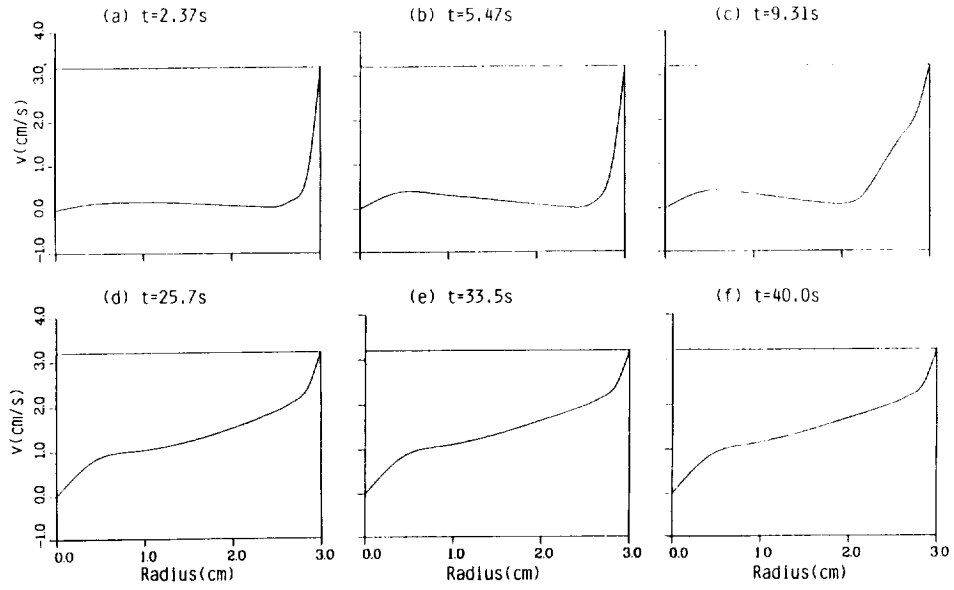

Fig. 7. Transient circumferential velocity profiles with respect to time and radial coordinate along $\theta = 180°$ (deceleration zone) at height $z = 1$ cm and $\omega = 10.2$ rpm, for oblique gravitational acceleration ($\psi = 60°$).

magnitude of cylindrical wall velocity near the end walls. (d) The introduction of acceleration flow driven by oblique gravitational acceleration in the acceleration zone cause a peculiar outflow in the region of $90^\circ < \theta < 270^\circ$ and inflow in the region of $90^\circ > \theta > 270^\circ$, particularly pronounced within the locations of $r/R < 0.5$ in r–z plane to satisfy the mass conservation (see Fig. 5). This peculiar dynamics of the coexistence of inflow and outflow initiate at the beginning of impulsive spin-up from rest and continue even after the status of steady-state. Figure 6 shows the appearance of negative circumferential component of velocity from the radial coordinate near the solid wall of container, propagating inward toward the center of rotating axis, and ending with maximum negative circumferential velocity located at $r = 0.4$ cm after the status of steady state condition. During the entire course of spin-up from rest, the maximum negative circumferential component of velocity appear in the time $8.5\,\mathrm{s} > t > 4.5\,\mathrm{s}$ with a value of -1.3 cm/s. (c) During the entire course of spin-up from rest to the status of steady-state condition, there is no fluid flow at the center of rotating axis for flow with normal gravitational acceleration, whereas there is always the flow across the center of rotating axis for flow with oblique gravitational acceleration (inflow in the region of $90^\circ > \theta > 270^\circ$, and outflow in the region of $90^\circ < \theta < 270^\circ$). (f) For the flow of spin-up from rest, the flow velocity in circumferential component increases gradually from the endwall and propagates inward toward the center of rotating axis. The final flow profile of solid rotation is nothing but a linear relation of $v = r\omega$ for flow with normal gravitational acceleration.

Initiation and development of reverse flow zones and Ekman layer were also computed. It shows that there is no apparent reverse flow zone shown for spin-up from rest with oblique gravitational acceleration. Figures 8 and 9 show the animation of Ekman layer at lower half r–z plane along $\theta = 0^\circ$ (acceleration zone), and $\theta = 180^\circ$ (deceleration zone), respectively, at $r = 2.40$ cm for spin-up from rest with oblique gravitational acceleration. Comparison of Figs. 3 and 8, 9 for the animation of initiation, development and decay of Ekamn layer profiles of spin-up from rest with gravitational accelerations along normal and oblique directions, respectively, can draw the following conclusions: (a) In r–z plane, Ekman layers which develop in the upper half and the lower half zones are same and are basically the flow profiles with mirror reflection. (b) For the flow of spin-up from rest with normal gravitational acceleration, animation of Ekman layer along $\theta = 0^\circ$ and 180° in r–z plane are same and basically the flow profiles with mirror reflection. (c) For the flow of spin-up from rest with oblique gravitational acceleration, animation of Ekman layer along $\theta = 0^\circ$ (acceleration zone) and $\theta = 180^\circ$ (deceleration zone) in r–z plane are entirely different. (d) For the development of temporary reverse flow zones near the sidewalls at the beginning of container spin-up from rest which decay quickly before the flow attain to solid-rotational states flow with normal gravitational acceleration is generated due to the fact of well-organized flow patterns with momentum transfer from the outer solid wall which propagate inward toward the center of rotating axis. This well-organized flow pattern has never occurred for flow with oblique gravitational acceleration which drives the flow with one-side accelerating, and the other side decelerating. This fairly asymmetric flow pattern with oblique gravitational acceleration provides no contribution to the generation of reverse flow zone which appear in the other case with symmetric flow pattern with normal gravitational acceleration. (e) Initiation and development of Ekman layer at the

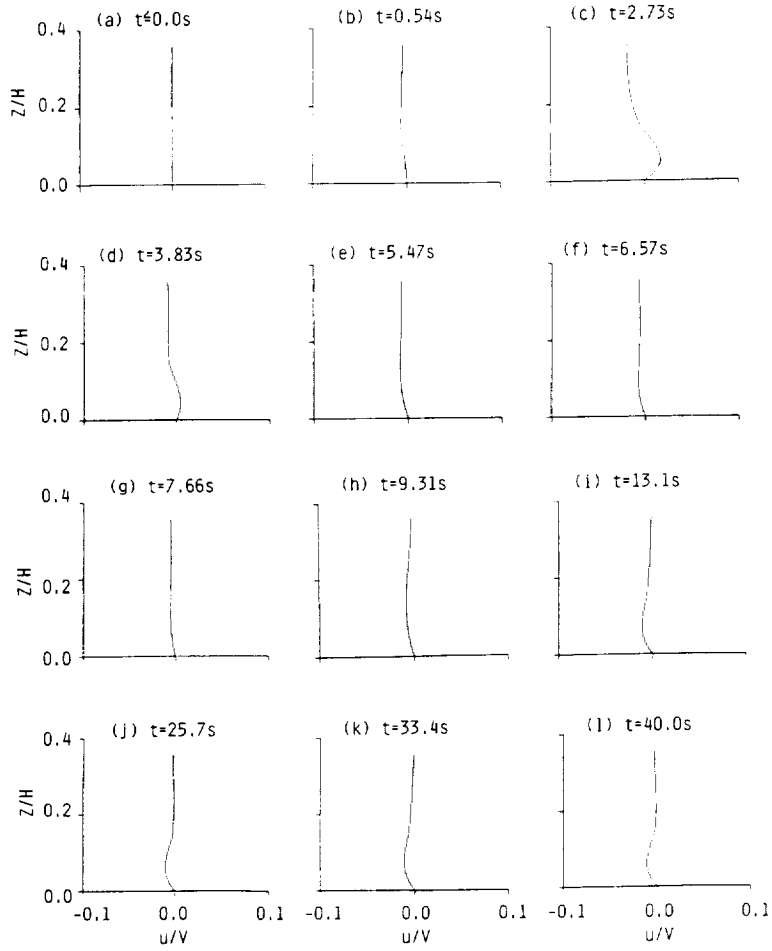

Fig. 8. Animation of the development of Ekman layer along $\theta=0°$ (acceleration zone) near the end wall of container in r–z plane at $r=2.40$ cm and $\omega=10.2$ rpm for oblique gravitational acceleration ($\psi=60°$).

beginning of flow spin-up from rest with normal gravitational acceleration are introduced because mass conservation requires a fill in of mass in positive radial direction due to the fluid mass spin-up near the sidewall of container at the beginning together with a sharp pressure gradient $\partial p/\partial r$ which is developed right after the impulsive start from rest generating radial component of flow toward lower pressure side. Ekman layer flow pattern decay quickly before flow reach to the equilibrium status of solid rotation. (f) Initiation and development of Ekman layer for spin-up flow from rest with oblique gravitational acceleration results in an entirely different story. A constant existence of velocity hill and velocity ditch along the radial direction, which even continues at the steady-state, makes the existence of Ekman layer without decay for flow with oblique gravitational acceleration. (g) At the deceleration side ($\theta=180°$) of spin-up flow with oblique gravitational acceleration, a constant existence of circumferential component

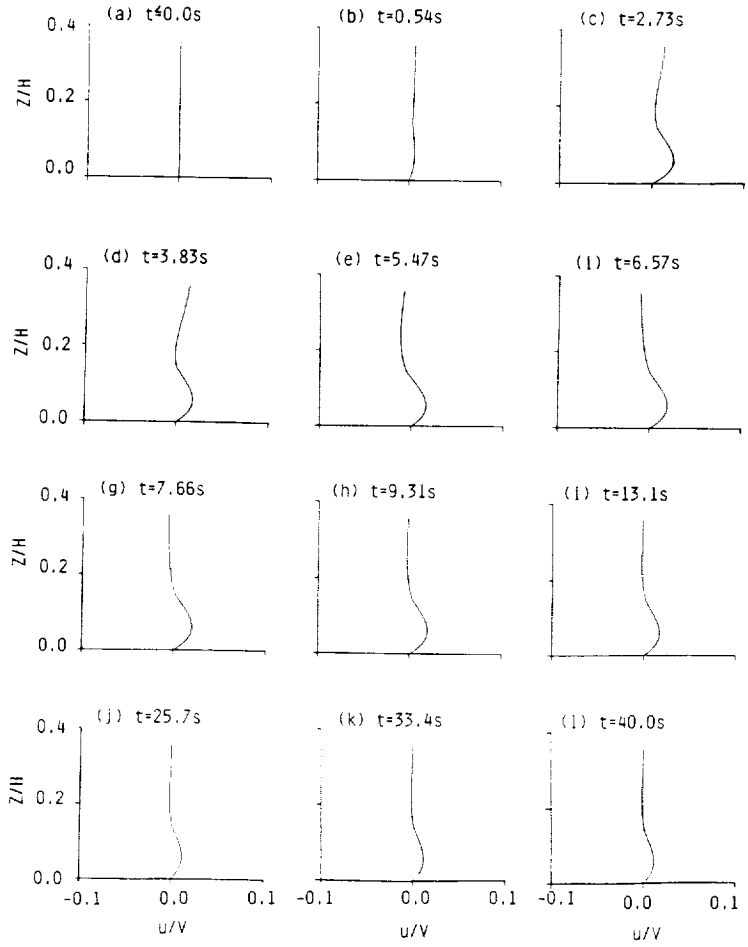

Fig. 9. Animation of the development of Ekman layer along $\theta=180°$ (deceleration zone) near the endwall of container in r–z plane at $r=2.40$ cm and $\omega=10.2$ rpm for oblique gravitational acceleration ($\psi=60°$).

velocity ditch near the endwall at $r=2.40$ cm, even after the flow attaining the status of steady state, results in a long lasting appearance of Ekman layer. It shows a peak (maximum peak value with $u/V=0.02$) positive radial velocity (positive radial velocity is contributed by the circumferential component of velocity ditch while negative radial velocity is due to the circumferential component of velocity hill at the corresponding location) located at $z/H=0.04$. (h) At the acceleration side ($\theta=0°$) of spin-up flow with oblique gravitational acceleration, flow pattern of Ekman layer is quite complicated. There is a circumferential component velocity ditch near the end wall at $r=2.40$ cm with spin-up from rest at the beginning of impulsive start to time at $t<5.2$ s which results in Ekman layer with positive radial component velocity with peak value located at $z/H=0.04$. After the time of $t>5.2$ s, a circumferential component velocity hill is gradually developed at $r=2.40$ cm which contributes to the development of negative

radial component velocity Ekman layer with peak value also located at $z/H=0.04$.

4. Discussion and Conclusions

Transient flow profiles of impulsive spin-up from rest in a filled cylinder have been studied numerically. A symmetric flow profile has been resulted with gravitational acceleration acting along the rotating axis of cylinder whereas an asymmetric with complicated flow profiles is obtained with oblique gravitational acceleration activated on the rotating container with respect to rotating axis. It is suggested that a finer size of grid points shall be adopted for flow field with higher Reynolds number for the purpose to avoid the generation of numerical instabilities associated with flow field computation.

A status of solid rotation can be reached for a symmetric flow field of impulsive spin-up from rest with gravitational acceleration acting along the rotating axis of container. There is a steady-state, but not a status of solid rotation with an asymmetric flow field for impulsive spin-up from rest with oblique gravitational acceleration acting on the flow fields. A temporary reverse flow zone can be developed at the beginning of spin-up before reaching the status of solid rotation with a symmetric flow field for higer Reynolds number flows. This temporary reverse flow zone can be missed for lower Reynolds number flow and also liquid rotation with asymmetric flow.

Ekman layer is developed during the course of impulsive spin-up from rest. This flow pattern is induced due to a sharp pressure gradient $\partial p/\partial r$ which drives a radial component flow toward the lower pressure side, and is terminated before the flow reaches the status of solid rotation with a symmetric flow profile spin-up from rest. The profiles of Ekman layer become fairly complicated with both positive and negative radial mass flow rates varying with respect to time coexistence with circumferential velocity ditch and velocity hill which appear jointly in the asymmetric rotating flow. A thorough understanding of these flow field can contribute greatly to a better design of spacecraft flow system, and also payload system of projectiles.[3,18]

Acknowledgement

The authors appreciate the support received from the NASA Grant NAG8-938 and NASA Contract No. NAS8-38609/Delivery Order No. 103.

References

1) Hung, R. J., Shyu, K. L. and Lee, C. C.: Medium Frequency Impulsive Thrust Excited Slosh Waves During Propellant Reorientation with Geyser, *J. Propul. Power*, **8** (1992), pp. 778–785.
2) Hung, R. J., Shyu, K. L. and Lee, C. C.: Liquid Hydrogen Slosh Wave Excited by Constant Reverse Gravity Acceleration of Geyser Initiation, *J. Spacecr. Rockets*, **29** (1992), pp. 523–528.
3) Hung, R. J., Lee, C. C. and Leslie, F. W.: Spacecraft Dynamical Distribution of Fluid Stresses Activated by Gravity Jitter Induced Slosh Waves, *J. Guid. Control Dyn.*, **15** (1992), pp. 817–824.

4) Hung, R. J., Lee, C. C. and Leslie, F. W.: Similarity Rules in Gravity Jitter Related Spacecraft Liquid Propellant Slosh Waves Excitation, *J. Fluids Struct.*, **6** (1992), pp. 493–522.
5) Hung, R. J., Lee, C. C. and Leslie, F. W.: Effect of the Baffle on the Spacecraft Fluid Propellant Viscous Stress and Moment Fluctuations, *Trans. Japan Soc. Aero. Space Sci.*, **35** (1993), pp. 187–207.
6) Hung, R. J., Lee, C. C. and Leslie, F. W.: Effect of the Baffle on the Asymmetric Gravity Jitter Excited Slosh Waves and Spacecraft Moment and Angular Fluctuations, *J. Aerosp. Eng.*, **207** (1993), pp. 105–120.
7) Hung, R. J., Pan, H. L. and Leslie, F. W.: Gravity Gradient or Gravity Jitter Induced Viscous Stress and Moment Fluctuations in Microgravity, *Fluid Dyn. Res.*, **14** (1994), pp. 29–51.
8) Hung, R. J., Pan, H. L. and Leslie, F. W.: Fluid System Angular Momentum and Moment Fluctuations Driven by Gravity Gradient or Gravity Jitter in Microgravity, *J. Flight Sci. Space Res. (ZFW)*, **18** (1994), pp. 195–202.
9) Hung, R. J., Pan, H. L. and Long, Y. T.: Sloshing Dynamics Modulated Cryogenic Helium Fluids Driven by Gravity Gradient of Jitter Accelerations Associated with Slew Motion in Microgravity, *Acta Mechanica Sinica*, **10** (1994), pp. 367–381.
10) Hung, R. J., Pan, H. L. and Long, Y. T.: Peculiar Behavior of Helium II Disturbances Due to Sloshing Dynamics Driven by Jitter Accelerations Associated With Slew Motion In Microgravity, *Cryogenics*, **34** (1994), pp. 641–648.
11) Wilkinson, D. T., Bender, P. L., Eardley, D. M., Gaisser, T. K., Hartle, J. B., Israel, M. H., Jones, L. W., Partridge, R. B., Schramm, D. N., Spapiro, I. I., Vessort, R. F. C. and Wagoner, R. V.: Gravitation, Cosmology and Cosmic-Ray Physics, *Phys. Today*, **39** (1986), pp. 43–46.
12) Kitchens, C. W., Jr., Gerber, N. and Sedney, R.: Spin Decay of Liquid-Filled Projectile, *J. Spacecr. Rockets*, **15** (1978), pp. 348–354.
13) Kitchens, C. W., Jr.: Navier-Stokes Equations for Spin-Up in a Filled Cylinder, *AIAA J.*, **18** (1980), pp. 929–934.
14) Stewartson, K.: On the Stability of Spinning Top Containing Liquid, *J. Fluid Mech.*, **5** (1959), pp. 577–592.
15) Hung, R. J., Long, Y. T. and Pan, H. L.: Sloshing Dynamics Induced Angular Momentum Fluctuations Driven by Jitter Accelerations Associated with Slew Motion in Microgravity, *Trans. Japan Soc. Aero. Space Sci.*, **37** (1994), pp. 217–234.
16) Hung, R. J. and Pan, H. L.: Asymmetric Slosh Wave Excitation in Liquid-vapor Interface Under Microgravity, *Acta Mechanica Sinica*, **9** (4) (1993), pp. 298–311.
17) Hung, R. J. and Pan, H. L.: Differences in Gravity Gradient and Gravity-Jitter Excited Slosh Waves in Microgravity, *Trans. Japan Soc. Aero. Space Sci.*, **36** (1993), pp. 153–169.
18) Hung, R. J. and Pan, H. L.: Fluid Force Activated Spacecraft Dynamics Driven by Gravity Gradient and Jitter Accelerations, *J. Guid. Control Dyn.*, **18**, in press (1995).
19) Hung, R. J. and Pan, H. L.: Effect of Baffle on Sloshing Modulated Torques Responsed to Orbital Accelerations in Microgravity, *J. Spacecr. Rockets*, **31**, in press (1995).
20) Hung, R. J. and Pan, H. L.: Rotational Speed and Wrapping of Different Size Cryogenic Helium Bubbles Around Dewar Well in Microgravity, *Aeronaut. J.*, in press (1995).
21) Hung, R. J. and Long, Y. T.: Baffle Effect of Cryogenic Helium Sloshing Dynamics in Response to Lateral Impulsive Acceleration in Microgravity, *Cryogenics*, in press (1995).
22) Holton, J. R.: *An Introduction to Dynamic Meteorology*, 2nd Edition, Academic Press, London, 1979, pp. 1–391.